🔓Open Access

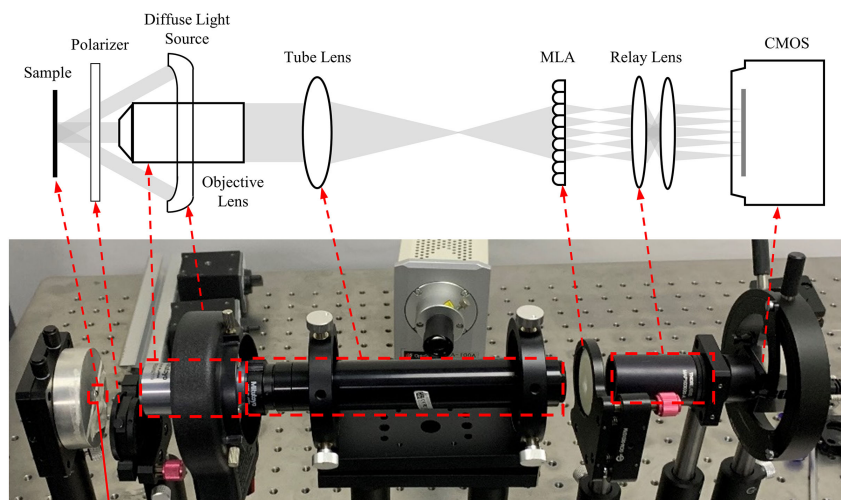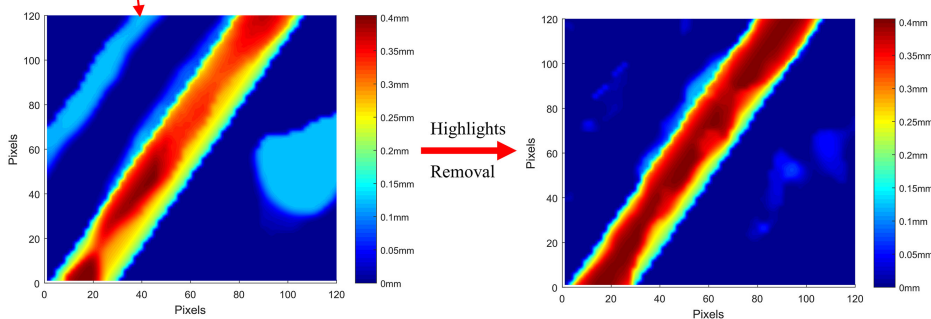# Three-dimensional Measurement of Specular Surfaces Based on the Light Field

Panyu Zhou
Lingbao Kong
Xiang Sun
Min Xu

3D Measurement of Specular Surfaces Based on the Light Field

Three-dimensional Measurement of Specular Surfaces Based on the Light Field

Panyu Zhou,[1] **Lingbao Kong** ⓘ**,**[1] **Xiang Sun** ⓘ**,**[1,2] **and Min Xu**[1,2]

Shanghai Engineering Research Center of Ultra-Precision Optical Manufacturing, Fudan University, Shanghai 200433, China
Academy for Engineering & Technology, Fudan University, Shanghai 200433, China

Abstract: As an important branch of computational optics, the light field can simultaneously record the spatial intensity and propagation direction of light, which provides a new way to realize three-dimensional (3D) measurement. Although light field measuring system (LFMS) can quickly detect nontransparent surfaces, specular light affects the overall measurement result. In this paper, an LFMS based on a diffuse light source and polarization technology is proposed to eliminate specular light and obtain a more accurate 3D reconstruction result in one exposure. During the measurement, a series of images corresponding to continuously varying polarization angle are captured, in which the value(V)-channel value distribution is used as the criterion of specular light removal efficiency, and hence, the image at the optimal polarization angle is obtained, in which the influence of specular light is removed. The depth map and specular light removal efficiency are experimentally compared with those of the traditional LFMS. The experimental results show that the depth map error can be greatly reduced, which further verifies the feasibility of the proposed method and system. The present study can be extended to the traditional optical system or other machine vision measurement methods involving specular light.

Index Terms: Light field, 3D measurement, specular surface, polarization, image processing.

1. Introduction

Common methods for detecting microstructures can be divided into contact measurement and non-contact measurement. Contact measurement uses the interaction between a mechanical probe and the tested surfaces to realize the detection of the surface, the detection accuracy of which is relatively high. Nevertheless, contact measurement may damage the surface of optical components, and the detection speed is relatively slow. Noncontact measurement uses light as a probe, which avoids the damage to the surface caused by contact, maintains the high precision and realizes a fast speed. The typical noncontact detection systems are white light interferometers and confocal microscopes. Nevertheless, these two detection systems require a scanning process to achieve 3D reconstruction so cannot realize real-time 3D surface reconstruction and detection.

In 1903, Ives [1] proposed a method by using grating to record the propagation of light, which is considered as the prototype of light field imaging. And then, in 1908, Lippmann [2] optimized the model and proposed that the use of microlens array can replace grating to record light field. In 1939, Gershun [3] for the first time, put forward the concept of 'light field', which can be used to describe the propagation of light in space. In 1991, Adelson and Bergen [4] proposed a seven-dimensional function as a quantitative presentation of light, including three spatial coordinate parameters, two angular parameters, wavelength and light propagation time. Then, in 1996, Levoy and Hanrahan [4] simplified the function to four parameters and put forward a model of light field defined by two planes, called 4D light field model, which is the foundation of light field research of recent years. Since then, many applications appeared, such as light field camera and camera array, etc. Based on this, Levoy *et al.* [5] proposed a light field microscope in 2006, which is generally applied in biological observation. This provides a noncontact measurement approach for microstructures.

Currently, light field microscopy is still under development for applications in nontransparent observation. The main difference between the observation of nontransparent surfaces and biological samples lies in the construction of the light source. In general, a transmission light source is used for biological observation, whereas a reflection light source is used for the observation of nontransparent samples. However, the introduction of reflected light may cause the problem of specular light. When the light intensity through the lens system is too strong, the sensor is overexposed, which will lead to loss of information in the region and eventually result in incomplete 3D information restoration or even reconstruction errors. Therefore, there is a need for effective methods to recover the specular areas.

In the open literature, it is known that the elimination of specular phenomena is mainly based on the two-color reflection model and the polarization model. In 1985, Shafer [6] proposed the two-color reflection model, and separated the specular reflection component with this model. Based on this, Klinker *et al.* [7] found that diffuse and specular pixels present a T-shaped distribution in the RGB color space and achieved highlight removal by separating the color vector into the object surface vector and the light source color vector. Later, Schluns and Teschan [8] extended the model from RGB color space to YUV color space and improved the effect of highlight removal. In 1990, Buelthoff *et al.* [9] proposed the shape-from-X (SFX) method for integrating different depths, and SFX can eliminate some specular areas; however, a series of pictures from different angles need to be taken for the calculation. In 1996, Bajcsy *et al.* [10] proposed the concept of S-space for analyzing the brightness, chroma, and saturation of colors and concluded that a highlight area could be detected and separated based on the phenomenon that the highlight would cause brightness enhancement and saturation reduction. Other researchers have proposed some other methods. Miyazaki *et al.* [11] utilized a combination of polarization-reflection models and rendering methods to fill in the highlight region. Tappen *et al.* [12] used pixel color information and a pixel gradient classifier to restore the diffuse component of an image. Mallick *et al.* [13] made use of the information of the nonspecular pixels at the edge of the specular region to eliminate the specular component of each pixel in the specular region through PDE iteration. Pesal *et al.* [14] used PCA and histogram equalization to quickly remove highlights. Zhang *et al.* [15] removed specular shading by adjusting the chroma of the color region and applying the de-specular algorithm to the SFS (shape from shading) algorithm. In 2004, Markus *et al.* [16] proposed phase measuring deflectometry (PMD) to measure specular surfaces based on a phase-shift algorithm, which realized high precision measurement of specular surfaces.

In 2005, Oliver *et al.* [17] proposed a method by fitting three parameters (intensity, degree of polarization and angle of polarization) from several images and acquired 3D measurement by relaxation algorithm. In 2017, Sun *et al.* [18] proposed the algorithm based on component separation and priority region filling theory to remove the highlights areas of smooth surfaces. In 2018, Niu *et al.* [19] proposed an advanced PMD method to get the depth map from absolute phase instead of integrating gradient data, and acquired 3D measurement of discontinuous specular surfaces. In 2019, Cai *et al.* [20] put forward an infrared-PMD method to reduce the 3D measurement affected by the external environment in actual measurements. However, for micro-nanostructures that contain diffuse regions, surfaces textures are lost in the reconstruction. This indicates that there
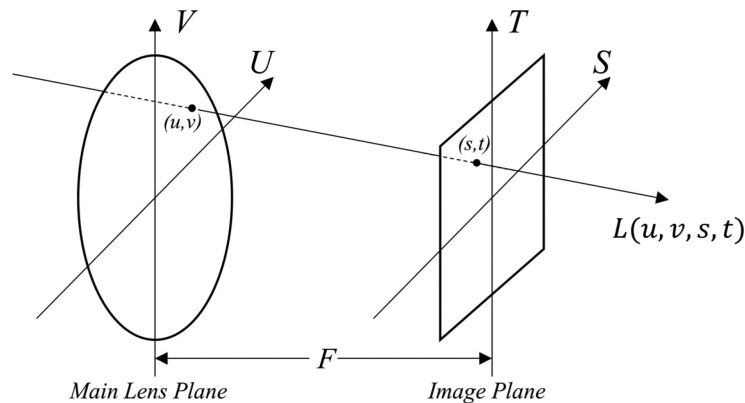
Fig. 1. Schematic diagram of the four-dimensional light field function based on two planes.

is much research work to be undertaken on highlight elimination; moreover, additional software operation time is necessary, and therefore, the overall measurement efficiency is greatly decreased.

In this paper, polarization technology combined with a diffuse light source is used to effectively eliminate the specular areas in a measurement based on the light field. The theoretical background and experimental studies regarding the proposed method will be explained in detail. Results and discussions will also be provided. The experimental results show that the proposed method is easy to operate and can physically eliminate highlights. Meanwhile, the overall measurement accuracy of the proposed method is improved.

2. Fundamentals in Light Field Measurement

2.1 Light Field Imaging

The original description of the light field was a seven-dimensional function that contained three positional parameters, two angular parameters, a parameter that defined the wavelength of the light and a parameter that defined the time of light travel [21]. For each ray, the wavelength and travel time can be regarded as fixed parameters in one exposure, so the light field function can be simplified to a five-dimensional function [22]. Different from the above representation of the light field, the light field can also be defined as the coordinates of the intersection of points on two parallel planes.

As shown in Fig. 1, a coordinate (U,V) on the main lens plane and a coordinate (S,T) on the image plane are established. Then, a sample of the light field between the lens and the sensor can be represented as L(u,v,s,t), and F is the focal length of the main lens.

In this way, the intensity distribution on the image plane of the imaging system can be represented by the ray integral of the light field.

$$I\ (s, t) = \iint L\ (u,\ v,\ s,\ t)\ du dv \tag{1}$$

In light field imaging, since the propagation direction is recorded, all the recorded rays can be projected onto a new plane at a different distance to form a new imaging plane to achieve refocusing. Fig. 2 shows the reverse tracing process of light field imaging. F represents the focal length of the main lens, and F' represents the refocus depth. Images of different depths can be reconstructed through this process.

The light ray passes through the main lens plane at (u,v) and the image plane at (s,t), and intersects the refocus plane at (s',t'). Take the reconstruction factor as α, so:
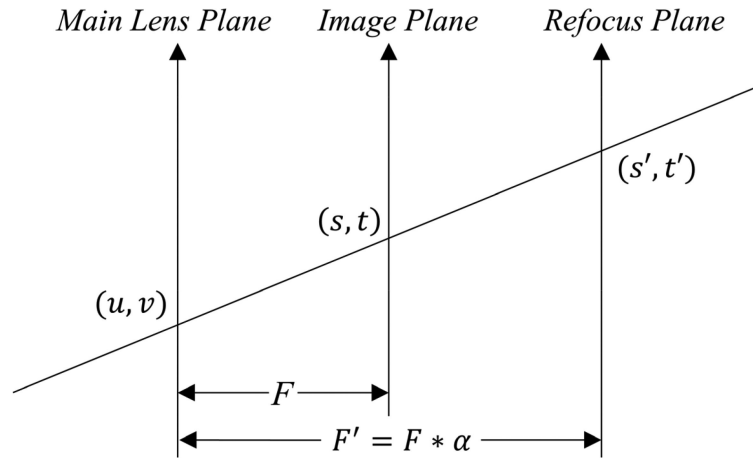
$$\alpha\ =\ \frac{F'}{F} \tag{2}$$

Fig. 2. Schematic diagram of the refocus progress of light field imaging.

According to the geometric relation, it can be deduced that:

$$\frac{F'}{F} = \frac{s' - u}{s - u} \tag{3}$$

Then, s can be expressed as:

$$s = u + \frac{s' - u}{\alpha} \tag{4}$$

and the relationship of s and t can be obtained from:

$$t = v + \frac{t' - v}{\alpha} \tag{5}$$

Assume that there is no attenuation of the light intensity during space propagation, L_F (u,v,s,t) is the light field on the image plane, and $L_{F'}$ (u,v,s',t') is the light field on the refocus plane, then:

$$L_{F'}\left(u, v, s', t'\right) = L_F\left(u, v, s, t\right) \tag{6}$$

Combining Eq. (2) to (6) generates:

$$L_{F'}\left(u, v, s', t'\right) = L_F\left(u, v, u\left(1 - \frac{1}{\alpha}\right) + \frac{s'}{\alpha}, v\left(1 - \frac{1}{\alpha}\right) + \frac{t'}{\alpha}\right) \tag{7}$$

Eventually, the intensity distribution of light field on the refocus plane can be calculated:

$$E_{(\alpha, F)}\left(s', t'\right) = \frac{1}{\alpha^2 F^2} \iint L_F\left(u, v, u\left(1 - \frac{1}{\alpha}\right) + \frac{s'}{\alpha}, v\left(1 - \frac{1}{\alpha}\right) + \frac{t'}{\alpha}\right) du dv \tag{8}$$

2.2 Eliminating the Specular Effect by Polarization

Nonetheless, affected by the nonuniformity of the light intensity distribution, specular reflection and diffuse reflection will occur at the same time on the tested surface when the image is captured by a system based on natural light. Normally, the specular reflection indicates the intensity distribution of the light source, and the diffuse reflection indicates the texture feature information of the tested surface. The mixing of the two kinds of reflected light leads to the overexposure in the image capture process of highly reflective surfaces, which may adversely affect the image quality. In polarization optics, light can be divided into p-type and s-type according to the polarization direction, and the reflection of p-type polarized light is eliminated at a certain angle. Usually, specular light reflected from the tested surface is polarized, and when it satisfies this angle, the reflection can
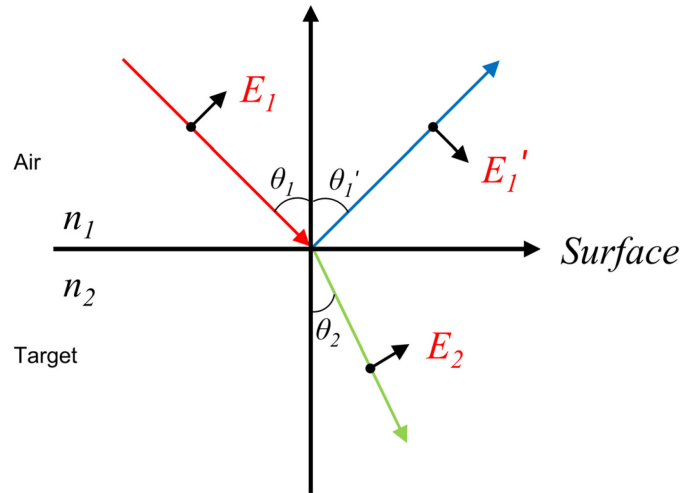
Fig. 3. Illustration of the polarization of natural light.

be eliminated. The refraction and reflection properties of p-type polarized light are shown in Fig. 3 based on the Fresnel polarization reflection principle.

In Fig. 3, the incident and refraction angles of p-type polarized light are θ_1 and θ_2, and the corresponding electric field intensities are E_1 and E_2. The electric field intensity of reflected light is E_1', and n_1 and n_2 are the refractive indexes of different light propagation media, respectively. If the reflective index of p-type polarized light is r_p, then:

$$r_p = \frac{E_1{'}}{E_1} = \frac{n_1 \cos \theta_2 - n_2 \cos \theta_1}{n_1 \cos \theta_2 + n_2 \cos \theta_1} = \frac{\frac{n_1}{\cos \theta_1} - \frac{n_2}{\cos \theta_2}}{\frac{n_1}{\cos \theta_1} + \frac{n_2}{\cos \theta_2}} \tag{9}$$

When $\theta_1 + \theta_2 = 90°$, the incident angle corresponding to p-type polarized light is complementary to the refraction angle, then $r_p = 0$, and the intensity of reflected p-type polarized light is equal to 0. The incident angle θ_1 is also called Brewster's angle. This state of polarized light is the optimal polarization state, and the corresponding specular reflection in the captured image of the object surface can be reduced to the minimum value. Therefore, a polarizer can be used to ensure that the light arrives at the sensor at the optimal polarization angle to eliminate the specular effect and obtain a more accurate 3D morphology of the surface to be measured.

3. Image Processing Algorithm

To establish a criterion to determine whether the pixels in images are overexposed, a suitable color space will be selected. It is known that image pixels can be divided into three different channels, and images can be separated into red (R), green (G) and blue (B) channels, also known as RGB color system. RGB includes almost all the colors that can be perceived by human vision, and it is one of the most widely used color systems. Nevertheless, the RGB color system defines images according to the combination of various colors, so it cannot distinguish the specular areas. Different from the RGB color system, the HSV color system consists of a hue (H) channel, a saturation (S) channel and a value (V) channel. For the light source, the V-channel value is related to the brightness of the illuminator, and for the object, it is related to the reflection ratio of the surface. Values usually range from 0(black) to 1(white). Therefore, the HSV color space is used instead of the RGB color space in this study.

Fig. 4 shows the flow chart of image processing in the light field measuring system (LFMS). The whole measurement process can be divided into image capture, image preprocessing and depth map acquisition. In the processing, an image is first captured by the system without a
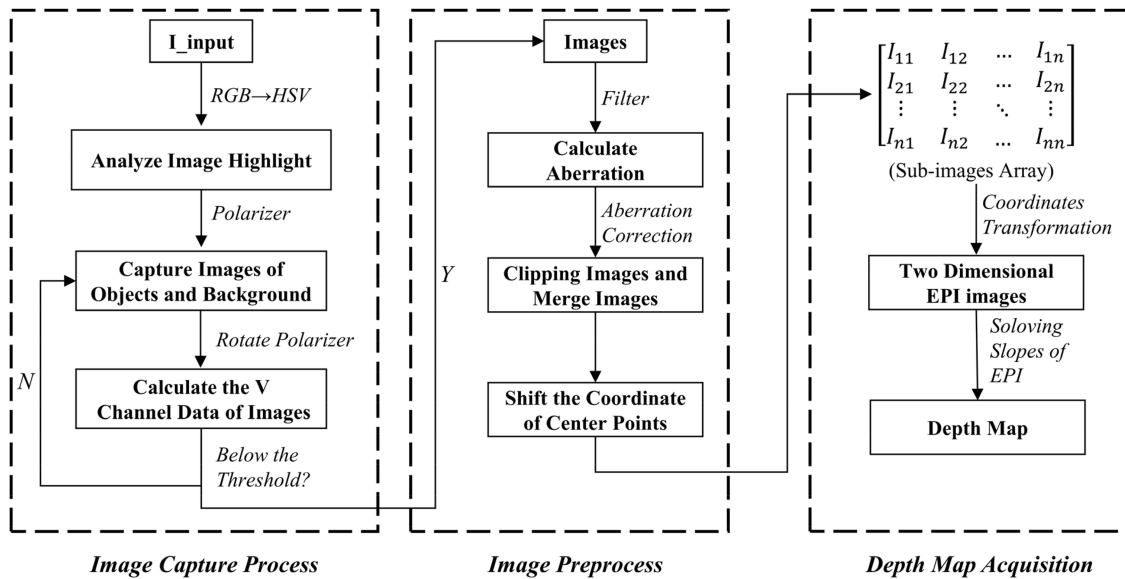
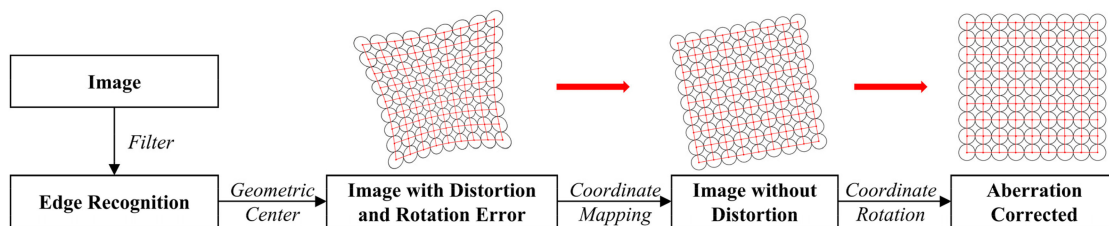Fig. 4. Flow chart of image processing in the LFMS.

Fig. 5. Flow chart of aberration removal.

polarizer, and the color space is converted from RGB to HSV. After the specular pixels of images are analyzed, a polarizer is introduced to further eliminate the specular light pixels. A series of images corresponding to different polarization angles are captured, and the V-channel value of each image is compared to the threshold value. The threshold value of images is determined by the cameras, which can be forecast based on the relationship between irradiance distribution of the light source and V-channel values. The threshold value of the camera used in the experiment is approximately 0.55. Pixels can be regarded as specular pixels if the V-channel value is higher than the threshold value. If the V-channel values are below the threshold, then specular pixels of the image can be eliminated. The average filter is used to increase the peak signal to noise ratio (PSNR) of images in which the V-channel values of pixels are below the threshold.

The installation of a microlens array (MLA) will introduce aberrations to the images captured by the LFMS, which are composed of a series of subimages. Hence, to eliminate the aberrations, it is necessary to analyze and correct each subimage captured by the MLA. Fig. 5 shows the flow chart of the aberration removal process. The edge information of sublens image is obtained as a circle by template matching calculation. The geometric centers of the identified circles are used as the centers of sublens. By connecting the centers of the recognized sublenses, a grid diagram related to the positions of sublenses can be obtained.

Generally, distortion and rotation errors are common aberrations existed in images. Distortion is generally divided into two types, radial distortion and tangential distortion [23]. Radial distortion
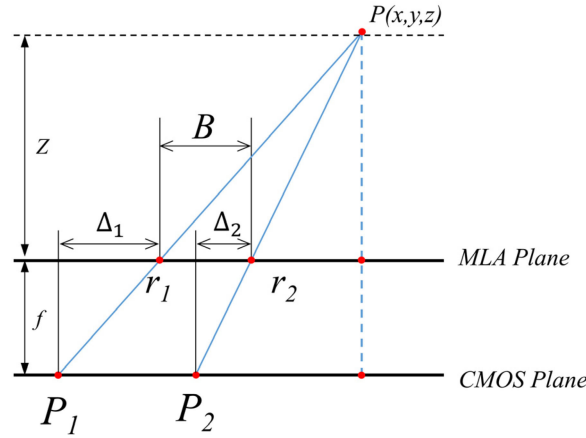
Fig. 6. Relationship between the depth and parallax.

refers to a position deviation along the radial direction of an image pixel centered on the distortion center, resulting in deformation of the image. Tangential distortion is caused by the lack of parallelism between the MLA plane and the CMOS plane, which will cause the tangential deviation of the image pixels. The distortions can be corrected by the following equations:

$$\begin{cases} x_{corrected} = x\left(1 + k_1 r^2 + k_2 r^4 + k_3 r^6\right) + p_2\left(r^2 + 2x^2\right) + 2p_1 xy \\ y_{corrected} = y\left(1 + k_1 r^2 + k_2 r^4 + k_3 r^6\right) + p_1\left(r^2 + 2y^2\right) + 2p_2 xy \end{cases} \tag{10}$$

where, x and y are the coordinates before correction, $x_{corrected}$ and $y_{corrected}$ are the coordinates after correction, r is the distance from the pixel to the distortion center, and k_1, k_2, and k_3 are the radial distortion coefficients, and p_1 and p_2 are tangential distortion coefficients.

For the image after aberration correction, the slope of the line connecting centers equals the rotation error of the image. Then, the rotation error can be eliminated by an affine transformation of the coordinate system.

Fig. 6 shows a schematic diagram of point P propagation onto the image plane through the MLA plane. r_1 and r_2 are the centers of microlenses. B is the distance between r_1 and r_2, Δ_1 and Δ_2 is the offset of P_1 and P_2. And $(\Delta_1 - \Delta_2)$ is the parallax of P. Z is the depth of point P, f is the distance between the MLA plane and CMOS plane.

Based on the geometric calculation, the relationship between parallax and depth can be expressed as:

$$Z = \frac{Bf}{\Delta_1 - \Delta_2} \tag{11}$$

Epipolar plane image (EPI) is used to arrange the images from different perspectives in the same row or the same column in order, and two-dimensional EPIs can be obtained [24]. By fixing a horizonal line in the image plane with constant y, we can get a horizonal EPI image shown in Fig. 7.

To extract the depth information of the target from the EPI image, the relationship between Δx and Δs can be deduced:

$$Z = f\frac{\Delta s}{\Delta x} \tag{12}$$

Fig. 7 shows a schematic diagram of the horizontal EPI. The depth of the object is related to the slope of the line between P_1 and P_2. Δs is the distance between the centers of two microlenses, and Δx is the parallax of P. S is the vertical coordinate of the image plane, and X is the horizontal coordinate of the CMOS plane. By solving the slope of the line corresponding to each point in the EPI, the depth map can be calculated according to Eq. (12).
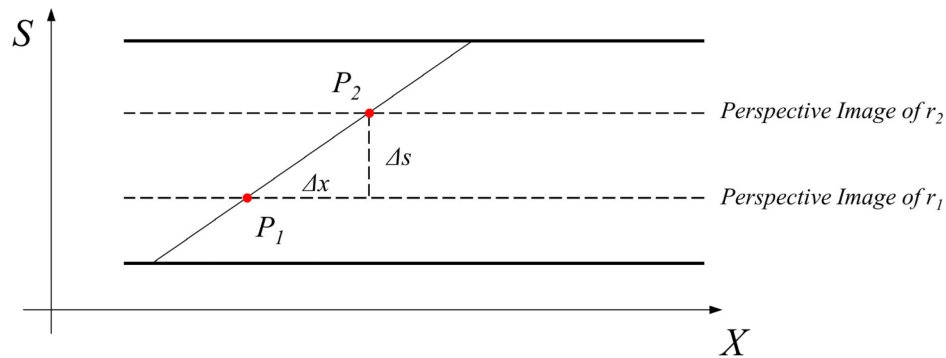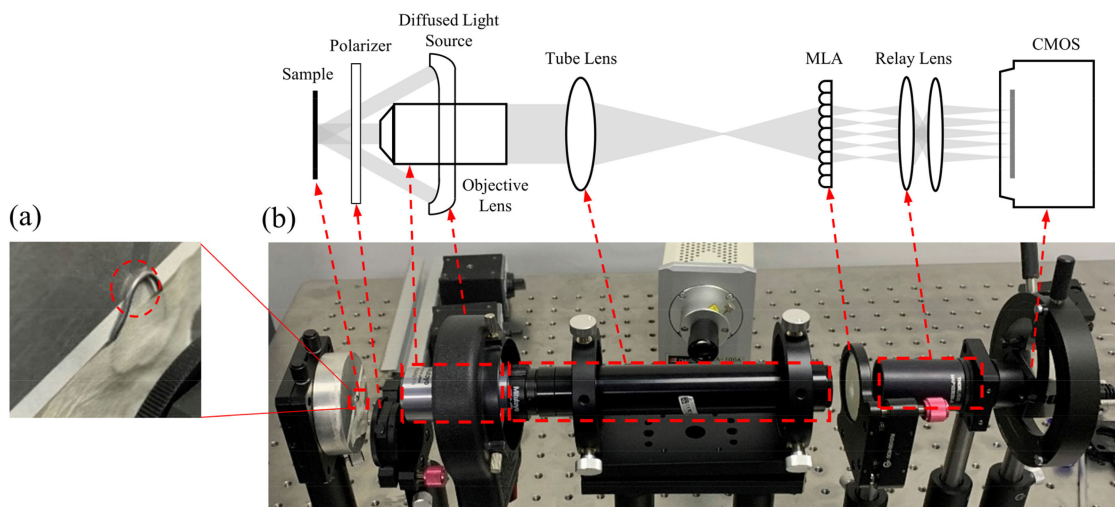
Fig. 7. Schematic diagram of horizontal EPI.

Fig. 8. (a) Sample to be measured; (b) LFMS based on a diffuse light source and polarization technology.

4. Experimental Studies

4.1 Experimental Setup

In the present study, an LFMS based on a diffuse light source and polarization technology is designed and established. The sample to be observed in the experiment is a small cut of a tin wire stick on a metallic surface as shown in Fig. 8(a). The experimental setup is shown in Fig. 8(b). The sample target is placed at 34 mm from the objective lens, which is the working distance of the objective lens in front of the system. A polarizer (GCL-05 from Daheng Optics, demountable) is placed between the objective lens and the sample. A 10X objective lens (Mitutoyo Plan Apo Infinity Corrected Long WD, from Edmund Optics) is used in the experiment, with a long working distance of 34 mm. The tube lens is an MT-4 from Edmund Optics, which is connected to the objective lens via a mechanical interface. The relay system used in this experiment is 1:1 with a focal length of 30 mm. The microlens array used is made from fused silica with a focal length of 5.1 mm, and the aperture of the microlenses is 300 μm. The selected camera is a CMOS (EO-4010 from Edmund Optics, with 4.19 mega-pixels). The diffuse light source is fixed on the objective lens by screws. The sample to be measured is illuminated by the diffuse light source, and the reflected light of the sample propagates through the objective lens and tube lens. The reflected light is focused on the focal plane of the objective lens. After the light passes through the microlens array, it is focused on the CMOS imaging plane, and then the light field images are acquired.
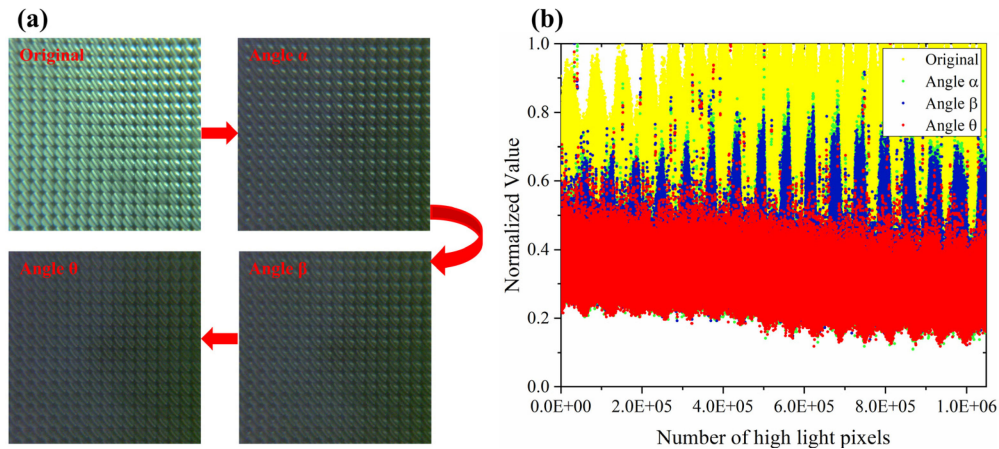
Fig. 9. (a) Original image and images taken at different polarization angles; (b) V-channel value distribution of each image.

For the proposed LFMS, the measured depth is related to the depth of field of the system, which can be calculated by [2]

$$\Delta = \frac{(2 + N^2)\,\lambda n}{2NA^2} \tag{13}$$

where, Δ is the depth of field of the LFMS, N is the quotient of the size of a microlens and the size of a pixel of the CMOS, λ is the wavelength of the illuminator, n is the refractive index of the objective space, and NA is the numerical aperture of the objective lens. According to Eq (13) and the system setup parameters, the measured step height or valley depth is 4.076 mm.

4.2 Results and Discussions

Several images have been captured by the modified LFMS as mentioned in the above section, including three images corresponding to different polarization angles and one original image (without the polarizer), as shown the in Fig. 9(a). Fig. 9(b) shows the V-channel value distribution of each image, where the X-axis represents the pixel number and the Y-axis represents the V-channel value of each pixel. From Fig. 9, it shows that the number of specular light pixels of the image decreases with the introduction of the polarizer. Angle θ can be taken as the optimal polarization angle since almost all the V-channel values of the pixels are below the threshold value.

To verify the specular effect removal efficiency of the polarizer, the V-channel value distribution and depth map of the original image and images taken at the optimal polarization angle are analyzed. Three rows of original images and images taken at the optimal polarization angle are sampled and analyzed, as shown in Fig. 10. The X-axis of Fig. 10(b) and Fig. 10(d) represents the pixel number of the same row from left to right, and the Y-axis represents the V-channel value of each pixel. Fig. 10(b) shows that nearly half of the pixels are overexposed in the original image, which indicates that the effect of the diffuse light source on specular removal is limited. However, with the introduction of the polarizer, the V-channel value distribution of the image taken at the optimal polarization angle is below the threshold value, as shown in Fig. 10(d).

By refocusing the original image and image taken at the optimal polarization angle, depth maps are obtained, as shown in Fig. 11. The coordinate axes represent the pixel in the image. In Fig. 11(b), there are two obvious regions of artifacts caused by specular reflection in the reconstructed result. Fig. 11(d) shows that the artifacts are removed, which indicates an improved reconstruction result.
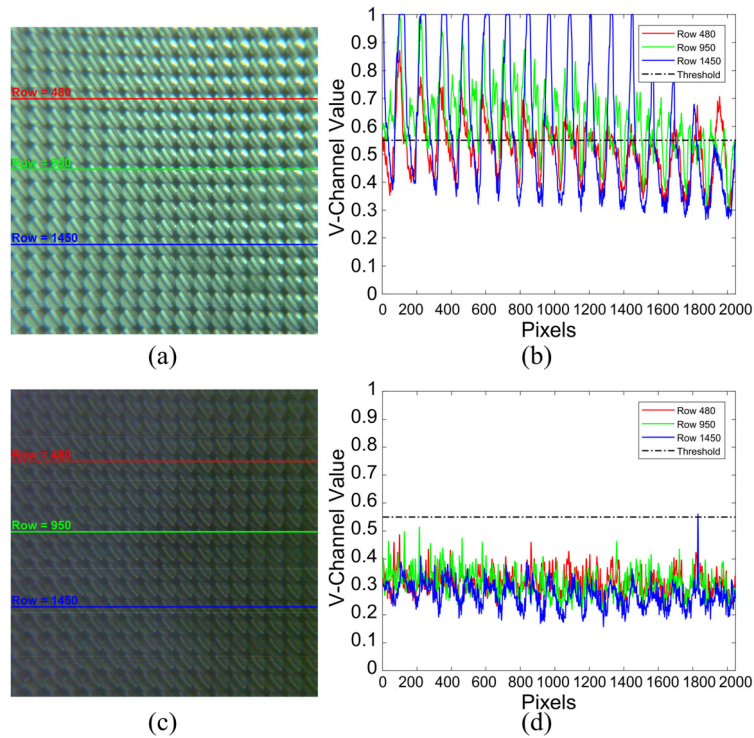
Fig. 10. (a) Original image taken without the polarizer; (b) V-channel value distribution of the original image; (c) Image captured at the optimal polarization angle; (d) V-channel value distribution of the image captured at the optimal polarization angle.
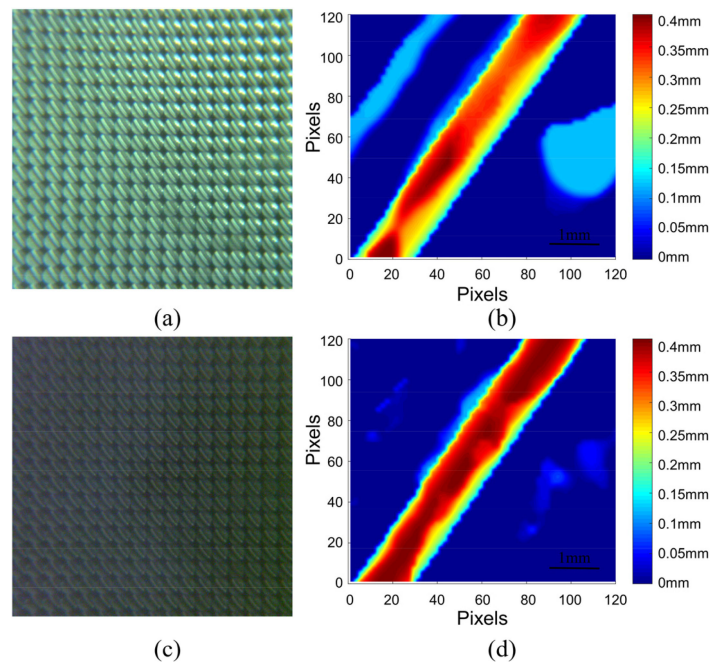

Fig. 11. (a) Image captured by the LFMS without the polarizer; (b) depth map of the tested sample(original); (c) Image captured at the optimal polarization angle; (d) depth map of the tested sample at the optimal polarization angle.
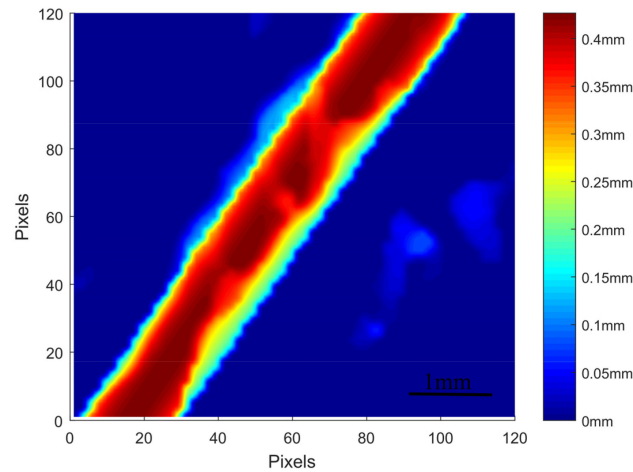
Fig. 12. Depth map of the tested sample obtained by the Keyence.

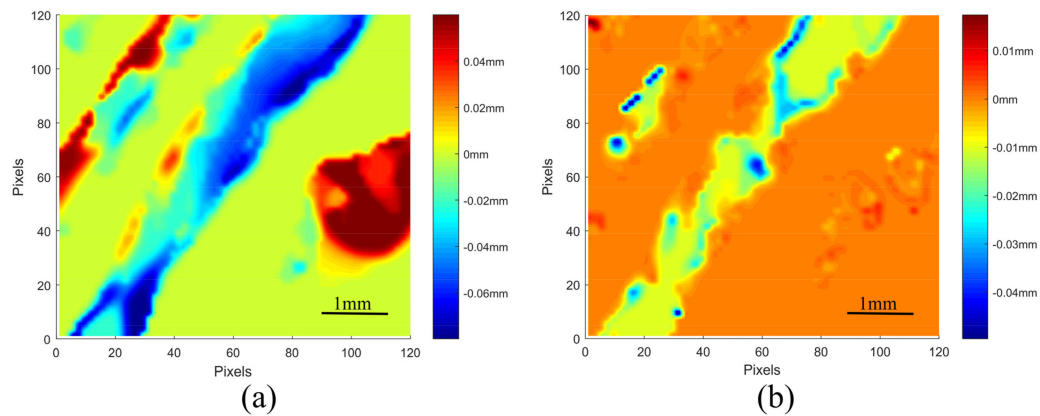(a)   (b)

Fig. 13. Residuals of the depth maps obtained (a) without the polarizer and (b) with the polarizer.

The test sample was also measured by a digital optical microscope with a large depth-of-field and advanced measurement capabilities named the Keyence VHX-5000, and the measured result is shown in Fig. 12, which will be used as a reference for comparison with the results obtained by the proposed system. By subtracting the reference (Fig. 12) from the two depth maps in Fig. 11(b) and (d), the residuals are used for precision comparison of the results measured without and with the polarizer in the LFMS, which are shown in Fig. 13. Fig. 13(a) shows the residuals for the depth map of the original image and the depth map obtained by the Keyence VHX-5000 digital microscope, while Fig. 13(b) shows that for the image taken at the optimal polarization angle.

In Fig. 13(a), there are higher residual error regions corresponding to the artifacts, which are the overexposed regions caused by specular light, while the residual errors are greatly reduced in Fig. 13(b), which indicates that a much better measurement result is achieved.

For a more precise comparison, areal surface parameters are calculated from the residual errors, as shown in Table 1. The peak to valley (PV) value is reduced from 139.9 μm to 67.0 μm, and the root mean square (RMS) value is reduced from 27.2 μm to 6.7 μm with the polarizer. This indicates that the LFMS based on diffuse light combined with polarization technology can greatly eliminate the influence of specular reflection and hence improve the reconstruction and measurement accuracy.

TABLE 1

Parametric Comparisons of the Measured Results With and Without the Polarization

Parameters	Without Polarization	With Polarization
PV(μm)	139.9	67.0
RMS(μm)	27.2	6.7

5. Conclusion

Highlights in the specular reflection of samples have an adverse effect on a light field measuring system (LFMS) and consequently affect the final reconstruction quality of the captured image. In this paper, an LFMS combining polarization technology and a diffuse light source is proposed to ensure that the 3D morphology can be obtained through a single exposure, and at the same time, the influence of highlights caused by the specular area is eliminated, which improves the overall measurement accuracy. At the same time, interpolation processing on the data is also avoided, which guarantees the accuracy of the whole measurement. A series of images corresponding to different polarization angles is captured by the proposed system, and then, the optimum polarization angle is obtained by analyzing the V-channel value distribution of each image; hence, a more accurate depth map can be obtained. Both the V-channel value distribution and depth map are used to verify the feasibility of the method. Experimental results show that the proposed LFMS can effectively eliminate specular light pixels and reduce depth map errors. The proposed method can be extended to the traditional optical microscope and other machine-vision measurement methods to address specular light.

References

[1] F. E. Ives, "Parallax stereogram and process of making same," U.S. Patent, 1903. 725,567.
[2] M. G. Lippmann, "Comptes rendus," *J. Phys.*, pp. 446–451, 1908.
[3] A. Gershun, "The light field," *J. Math. Phys.*, pp. 51–151, 1939.
[4] M. Levoy and P. Hanrahan, "Light field rendering," *Annu. Conf. Comput. Graph. Interactive Tech.,* 1996. pp. 31–42.
[5] M. Levoy and R. Ng., "Light field microscopy," in *Proc. SIGGRAPH*, 2006. pp. 924–934.
[6] S. A. Shafer, "Using color to separate reflection components," *Color Res. Appl.*, vol. 10, no. 4. pp. 210–218, 1985.
[7] G. J. Klinker, S. A. Shafer, and T. Kanade, "The measurement of highlights in color images," *Int. J. Comput. Vis.*, vol. 2, no. 1. pp. 7–32, 1988.
[8] K. Schlüns and M. Teschner, "Fast separation of reflection components and its application in 3D shape recovery," in *Proc. 3rd Color Imag. Conf.*, 1995. pp. 48–51.
[9] H. H. Buelthoff and L. Alan, "Shape-from-x: Psychophysics and computation," in *Proc. Sensor Fusion III: 3D Perception Recognit.*, 1991, Art. no. 1383.
[10] R. Bajcsy, S. W. Lee, and A. Leonardis, "Detection of diffuse and specular interface reflections and inter-reflections by color image segmentation," *Int. J. Comput. Vis.*, vol. 17, no. 3. pp. 241–272, 1996.
[11] D. Miyazaki, R. T. Tan, K. Hara, and K. Ikeuchi, "Polarization-based inverse rendering from a single view," in *Proc. IEEE Int. Conf. Comput. Vis.*, 2003. Art. no. 982.
[12] M. F. Tappen, W. T. Freeman, and E. H. Adelson, "Recovering intrinsic images from a single image," *IEEE Trans. Pattern Anal. Mach. Intell.*, vol. 27, no. 9, pp. 1459–1472, Sep. 2005.
[13] S. P. Mallick, T. Zickler, and P. N. Belhumeur, "Specularity removal in images and videos: A PDE approach," *Eur. Conf. Compu. Vis. (ECCV)*, 2006, pp. 550–563.
[14] P. Koirala, M. Hauta-Kasari, and J. Parkkinen, "Highlight removal from single image," in *Proc. Adv. Concepts Intell. Vis. Syst.*, 2009, pp. 176–187.
[15] Z. X., Y. Gao, and T. Caelli, "Color adjustment and specular removal for non-uniform shape from shading," in *Proc. Int. Conf. Digit. Image Comput Techn. Appl.*, 2010. pp. 563–568.
[16] M. C. Knauer, J. Kaminski, and G. Hausler, "Phase measuring deflectometry: A new approach to measure specular free-form surfaces," *Opt. Metrology Prod. Eng.*, 2004, Art. no. 5457.
[17] O. Morel, F. Meriaudeau, C. Stolz, and P. Gorria, "Polarization imaging applied to 3D reconstruction of specular metallic surfaces," in *Proc. SPIE*, vol. 5676, pp. 178–186, 2005.
[18] X. M. Sun, Y. Liu, X. Y. Yu, H. B. Wu, and N. Zhang, "Three-dimensional measurement for specular reflection surface based on reflection component separation and priority region filling theory," *Sensors*, vol. 17, no. 1, p. 215, 2017.
[19] Z. Q. Niu, N. Gao, Z. H. Zhang, F. Gao, and X. Q. Jiang, "3D shape measurement of discontinuous specular objects based on advanced PMD with bi-telecentric lens," *Opt. Express*, vol. 26, no. 2. pp. 1615–1632, 2018.
[20] C. X. Chang, Z. H. Zhang, N. Gao, and Z. Z. Meng, "Three-dimensional shape measurement of specular objects based on infrared phase-measuring deflectometry," in *Proc. SPIE, AOPC Opt. Sens. Imag. Technol.*, vol. 11338, 2019, p. 113381Y.

[21] E. H. Adelson and J. R. Bergen, "The plenoptic function and elements of early vision," *Comput. Models Vis. Process*, vol. 2, 1991.

[22] L. McMillan and G. Bishop, "Plenoptic modeling: An image-based rendering system," in *Proc. Annu. Conf. Comput. Graphic Interactive Techn.*, 1996. pp. 39–46.

[23] D. C. Brown, "Decentering distortion of lenses," *Photogrammetric Eng. Remote Sens.*, 1966.

[24] S. Wanner and B. Goldluecke, "Variational light field analysis for disparity estimation and super-resolution," *IEEE Trans. Pattern Anal. Mach. Intell.*, vol. 36, no. 3, pp. 606–619, Mar. 2014.